Reference dosimetry calculations for neutron capture therapy with comparison of analytical and voxel models

J. T. Goorley
Nuclear Reactor Laboratory, Massachusetts Institute of Technology, Cambridge, Massachusetts 02139, and Department of Radiology, Beth Israel Deaconess Medical Center, Harvard Medical School, Boston, Massachusetts 02115

W. S. Kiger III[a)]
Nuclear Reactor Laboratory, Massachusetts Institute of Technology, Cambridge, Massachusetts 02139, and Department of Radiation Oncology, Beth Israel Deaconess Medical Center, Harvard Medical School, Boston, Massachusetts 02115

R. G. Zamenhof
Department of Radiology, Beth Israel Deaconess Medical Center, Harvard Medical School, Boston, Massachusetts 02115

(Received 4 April 2001; accepted for publication 19 October 2001; published 25 January 2002)

As clinical trials of Neutron Capture Therapy (NCT) are initiated in the U.S. and other countries, new treatment planning codes are being developed to calculate detailed dose distributions in patient-specific models. The thorough evaluation and comparison of treatment planning codes is a critical step toward the eventual standardization of dosimetry, which, in turn, is an essential element for the rational comparison of clinical results from different institutions. In this paper we report development of a reference suite of computational test problems for NCT dosimetry and discuss common issues encountered in these calculations to facilitate quantitative evaluations and comparisons of NCT treatment planning codes. Specifically, detailed depth-kerma rate curves were calculated using the Monte Carlo radiation transport code MCNP4B for four different representations of the modified Snyder head phantom, an analytic, multishell, ellipsoidal model, and voxel representations of this model with cubic voxel sizes of 16, 8, and 4 mm. Monoenergetic and monodirectional beams of 0.0253 eV, 1, 2, 10, 100, and 1000 keV neutrons, and 0.2, 0.5, 1, 2, 5, and 10 MeV photons were individually simulated to calculate kerma rates to a statistical uncertainty of $<1\%$ (1 std. dev.) in the center of the head model. In addition, a ''generic'' epithermal neutron beam with a broad neutron spectrum, similar to epithermal beams currently used or proposed for NCT clinical trials, was computed for all models. The thermal neutron, fast neutron, and photon kerma rates calculated with the 4 and 8 mm voxel models were within 2% and 4%, respectively, of those calculated for the analytical model. The 16 mm voxel model produced unacceptably large discrepancies for all dose components. The effects from different kerma data sets and tissue compositions were evaluated. Updating the kerma data from ICRU 46 to ICRU 63 data produced less than 2% difference in kerma rate profiles. The depth-dose profile data, Monte Carlo code input, kerma factors, and model construction files are available electronically to aid in verifying new and existing NCT treatment planning codes.
[DOI: 10.1118/1.1428758]

I. INTRODUCTION

Neutron Capture Therapy (NCT) is a biologically targeted, binary radiation therapy for cancer that combines neutron irradiation with a tumor targeting agent labeled with a stable isotope having a high thermal neutron capture cross section and yielding charged particle reaction products after neutron capture.[1–3] Boron-10 has traditionally been the isotope of choice due to its very large thermal neutron capture cross section of 3840 barns,[4] a high Q value of 2.79 MeV, and densely ionizing disintegration products consisting of an alpha particle and a ^{7}Li recoil ion. Furthermore, these particles deposit their energies to within ~ 10 μm of the reaction site, potentially making the radiation highly cell selective. Equally important is the biochemical ability of the isotopically labeled compound to accumulate preferentially in tumor cells relative to normal tissue or blood,[5,6] since this uptake ratio determines the therapeutic advantage of NCT to a large extent. Preferential uptake of the ^{10}B compound by tumor cells enables the high LET particles from the $^{10}\mathrm{B}(n,\alpha)^{7}\mathrm{Li}$ reaction to be delivered with microscopic selectivity to the targeted cells.

The radiation delivered in NCT is a complex mixed field of high and low LET radiation that depends on the spatial, spectral, and angular characteristics of the incident neutron beam as well as on the geometry and elemental composition of the target itself. For treatment planning and dosimetry purposes, the radiation field is generally divided into four primary dose components: thermal neutron, fast neutron, photon, and ^{10}B dose. The thermal neutron dose primarily arises from the $^{14}\mathrm{N}(n,p)^{14}\mathrm{C}$ thermal neutron capture reac-

tion, which comprises 96% of the neutron kerma for ICRU 46 brain tissue[7] below the 0.5 eV energy cutoff for thermal neutrons. The fast neutron dose is primarily due to elastic neutron collisions with hydrogen, $^{1}H(n,n')^{1}H$, and represents 90% of the adult brain kerma between energies of ~600 eV and ~3 MeV. Other neutron reactions, primarily with ^{12}C, ^{16}O, and ^{31}P generally contribute 4%–8% to the brain kerma between ~40 eV and ~5 MeV, but at certain resonance energies may contribute more. The photon dose component originates from two sources, contaminating photons in the neutron beam incident on the target and prompt gammas produced by neutron capture in the target, principally by the $^{1}H(n,\gamma)^{2}H$ reaction in tissue. The ^{10}B dose arises primarily from the $^{10}B(n,\alpha)^{7}Li$ capture reaction with thermal neutrons. With preferential ^{10}B uptake by the tumor, a therapeutic advantage is achieved. In addition, the effective dose due to ^{10}B depends on the microdistribution of the boron compound,[8] the time after compound administration,[9] and each individual patient's physiology.[10,11]

The calculation of these four dose components is significantly more complicated than the determination of dose in conventional photon therapy, which generally relies on empirical algorithms based on in-phantom dose measurements.[12] Because of this complexity, it is generally believed that solution of the neutron transport equation[13] is required for accurate NCT treatment planning, typically using Monte Carlo methods. Deterministic transport methods such as the discrete ordinates, or S_n, method have also been applied to NCT treatment planning calculations.[14,15] Although efforts to develop empirical dose algorithms for NCT treatment planning have been made, the methods are not yet adequately developed for clinical application.[16]

To date, comparisons of NCT treatment planning software have been limited in scope and only to the three codes used clinically in the USA and Europe: MacNCTPlan,[17–19] developed at Harvard–Massachusetts Institute of Technology (MIT), BNCT_rtpe,[20,21] and its successor, SERA,[22] both developed at the Idaho National Engineering and Environmental Laboratory. The study by Goorley *et al.* demonstrated close agreement between the MacNCTPlan and BNCT_rtpe codes in evaluating a single clinical BNCT test case.[23] An extensive comparison between SERA and MCNP,[24] which is the ''transport engine'' used in MacNCTPlan, was recently completed for boron neutron capture synovectomy.[25] Other NCT treatment planning systems are being developed in Australia,[26] Italy,[27] and Japan,[28] but to date have not been described in the scientific literature or applied clinically.

Evaluation and comparison of treatment planning software is a critical step in the wider goal of standardization of dosimetry for NCT. Efforts to compare and standardize physical dosimetry in NCT have been formally initiated in the USA,[29] Europe,[30] and internationally.[31] As clinical trials of NCT progress, the benefits of standardized physical and computational dosimetry will permit the normalization of the dosimetry for subjects treated by NCT at different institutions and may eventually enable the legitimate pooling of such multisite clinical data.

Although different investigators have sometimes used widely different computational approaches in NCT treatment planning calculations, dose calculations based on the same problem description should produce the same results. In this paper, we propose a calculated set of reference depth-kerma rate profiles to be used as part of the verification and comparison of NCT treatment planning software. To provide reference computational dosimetry data that would be useful to other investigators, thermal neutron, fast neutron, induced photon, incident photon, and ^{10}B one-dimensional depth-kerma rate distributions were computed with high statistical precision along the central axis of a human head phantom. These kerma rate profiles were calculated for irradiation of the head phantom with monoenergetic and monodirectional neutron and photon beams of energies relevant to neutron capture therapy applications as well as for a ''generic'' broad spectrum epithermal neutron beam using the general purpose Monte Carlo radiation transport code MCNP (version 4B)[24] with the most up-to-date neutron and photon cross sections, material compositions, and kerma factors available. There is, however, no intent to claim that these data provide a ''gold standard,'' rather, this study represents a first step toward the objective standardization of computational dosimetry in NCT.

In addition to the reference calculations, in this paper we examine the effects of several modeling parameters on radiation transport and dosimetry. Since two of the NCT treatment planning codes used in clinical trials employ voxel representations (of different spatial resolution) to describe the phantom geometry and all three use voxels for tallying, the impact of voxel mesh size was evaluated by comparing dose-depth data computed in the analytical representation (i.e., using smooth geometric curves) of a head phantom with data computed in four voxel model representations of the same phantom with different voxel sizes. In addition, owing to the historically separate development of existing NCT treatment planning codes and the present lack of accepted standards for NCT dosimetry, different research groups have used different tissue densities and elemental compositions resulting in correspondingly different kerma values and radiation transport characteristics. The impact of these differences was evaluated and a unified set of kerma values based on ICRU 46 tissue compositions[7] is recommended. The impact of different approaches to treating the thermal neutron scattering law for hydrogen is examined. The significance of the thermal neutron flux depression due to absorption by ^{10}B in tissue is presented in the expanded version of this paper available with the electronic database that includes the depth-kerma rate profile data.

II. METHODS AND MATERIALS

The magnitudes of the effects of material composition, kerma factors, model mesh size, and beam energy on in-phantom dose profiles were evaluated using the general purpose Monte Carlo radiation transport code MCNP, version 4B.[24] The reference phantom model for these calculations is an analytical representation of the modified Synder head phantom.[32] Kerma rates were calculated in rectangular

prisms with a 16×16 mm cross section centered on the *z* axis and with 4 mm thickness in the *z* direction. To be strictly valid, comparisons should be made of the same tally volume, as kerma rates calculated for different volumes can yield different results. To provide a tally grid that consistently calculates kerma over the same volume for all models, tally cells in the analytical model were averaged axially as needed, and kerma rates in 8 and 4 mm cells in the voxel models were averaged laterally to agree with the 16×16 mm cross sections in the analytical model. Due to the symmetry of the modified Synder head phantom and the incident radiation fields about the *z* axis, the approach is equivalent to using a tally mesh with dimensions of 8×8 mm in the *x* and *y* directions with a voxel edge aligned with the *z* axis. Using the 16×16 mm cross section tally volume rather than a single one of the four 8×8 mm tally volumes aligned to the *z* axis provides an advantage of larger volume and hence improved tally statistics. The following sections describe the modified Snyder head phantom, construction of voxel models, material compositions, kerma factors, thermal neutron scattering treatment, and the photon and neutron source beams.

A. Modified Synder head phantom geometry

Recent efforts in physical dosimetry standardization have used a simple rectangular water phantom.[32] While a rectangular water phantom could be used to test the Monte Carlo transport calculations, a more realistic model, such as the Snyder head phantom,[32] with its curved surfaces, heterogeneous composition, and appropriate biological materials, is a more robust test of treatment planning software. An ellipsoidal head phantom based on the Snyder model is used by the Harvard–MIT group for physical dosimetry of the two neutron beams at the MIT Research Reactor.[33,34]

The original Snyder head phantom[31] consists of two ellipsoids, which divide the head into regions of cranium and adult brain. A third 5 mm thick shell representing skin has also been added.[35] Equations (1), (2), and (3), which locate the center of the head at the origin, specify these regions: the boundary between brain and skull:

$$\left(\frac{x}{6}\right)^2+\left(\frac{y}{9}\right)^2+\left(\frac{z-1}{6.5}\right)^2=1; \tag{1}$$

the boundary between skull and scalp:

$$\left(\frac{x}{6.8}\right)^2+\left(\frac{y}{9.8}\right)^2+\left(\frac{z}{8.3}\right)^2=1; \tag{2}$$

the boundary between scalp and air:

$$\left(\frac{x}{7.3}\right)^2+\left(\frac{y}{10.3}\right)^2+\left(\frac{z}{8.8}\right)^2=1. \tag{3}$$

These equations describe the phantom illustrated in Fig. 1.

B. Voxel models

Three voxel models of the Snyder head phantom were prepared with different mesh sizes. All voxel models were derived from a three-dimensional TIFF format image stack with a 1 mm in-plane resolution and a 2 mm slice width that represents the Snyder head model in the same way that a CT image stack represents patient geometry in a treatment planning calculation. The three voxel models were composed of cubic voxels, with edge lengths of 16, 8, and 4 mm, and were generated from this TIFF image stack using MATLAB (The Mathworks, Natick, MA) and FORTRAN programs. Each voxel contained a mixture of the 4 primary materials (air, skin, bone, or brain) in 10% increments, which resulted in 286 possible combinations of materials. Not all possible combinations were used in the models. A description of the voxel model generation and materials selection process is included in the expanded paper in the EPAPS[60] electronic database, as well as some of the model construction files, including the TIFF image stack. These three voxel models were verified to be similar in size and shape to the analytical model by superposing the cross sections of the analytical model (plotted with MCNP) over those of the voxel models, as shown in Fig. 2.

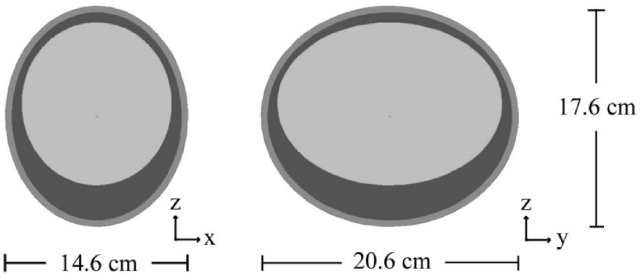

FIG. 1. Cross sections through the modified Snyder head phantom at the planes $y=0$ (left) and $x=0$ (right). The dimensions of the external shell are shown. The light gray central ellipsoid is composed of adult whole brain. The dark gray region is composed of adult cranium, and the medium gray region represents adult skin.

C. Tissue compositions

The three different regions of the analytical modified Snyder head phantom were composed of adult whole brain, adult whole cranium, and adult skin materials, as defined by ICRU

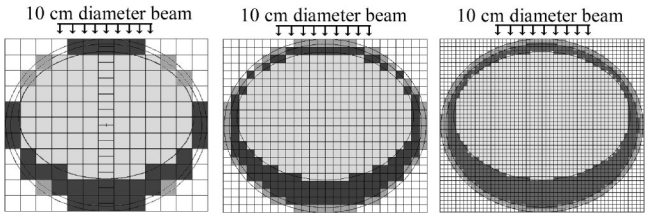

FIG. 2. A comparison of voxel and analytical models. The analytical model (curved lines) is superimposed over the 16 mm voxel model (left), the 8 mm voxel model (center), and the 4 mm voxel model (right). For clarity, the material mixtures are colored according to the most abundant primary material in the mixture. Brain is colored the lightest gray, bone the darkest gray, skin is medium gray, and air white. Additional segmentation for finer tally resolution is visible along the beam axis in the 16 mm voxel model. The beam axis in this figure corresponds to the *z* axis in Fig. 1.

TABLE I. Material densities and compositions in mass percent.

Z	Element	Air (Ref. 37)	ICRU 46 Skeleton–Cranium (Ref. 7)	ICRU 46 Adult whole brain (Ref. 7)	ICRU 46 adult skin (Ref. 7)
ρ (g/cm^3)		0.001 293	1.610	1.040	1.090
1	H	0	5.0	10.7	10.0
6	C	0.01	21.2	14.5	20.4
7	N	75.53	4.0	2.2	4.2
8	O	23.18	43.5	71.2	64.5
11	Na	0	0.1	0.2	0.2
12	Mg	0	0.2	0	0
15	P	0	8.1	0.4	0.1
16	S	0	0.3	0.2	0.2
17	Cl	0	0	0.3	0.3
19	K	0	0	0.3	0.1
20	Ca	1.28	17.6	0	0

46[7] and listed in Table I. Variation between individuals does exist, however.[36] Air, of composition described by Chadwick *et al.*,[37] surrounds the models.

Nitrogen and hydrogen are the two most important elements for neutron transport and dosimetry in the energy range of interest. Differences in nitrogen and hydrogen concentrations in tissue can produce substantial differences in calculated doses. In addition, variation in the hydrogen concentration can affect neutron transport due to its large cross section and high atomic density. Small changes in the nitrogen concentration will proportionally change the thermal neutron kerma factors, but will not significantly affect neutron transport because the nitrogen macroscopic cross section is small compared to that of hydrogen.

It is also important that the neutron capture and subsequent production of prompt gamma rays in various elements are modeled correctly. The ENDF60 cross section library[38] used in these Monte Carlo calculations provides pointwise continuous energy[24] cross sections derived from the ENDF/B-VI nuclear data library,[39] and includes the corresponding gamma production data.

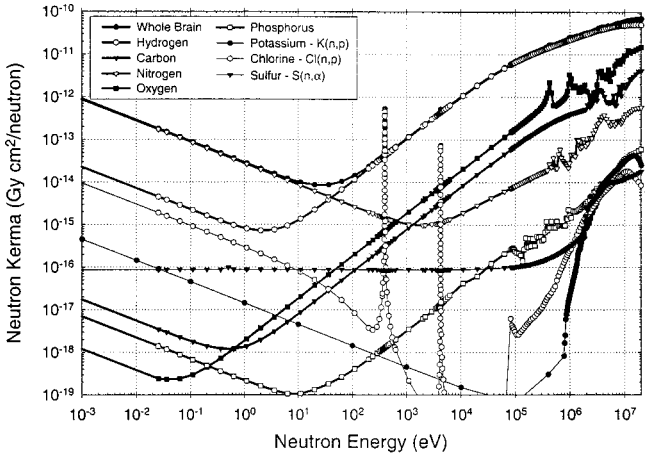

FIG. 3. Contributions to adult whole brain neutron kerma from different elements. All elemental kerma data is from ICRU 63, except for data for K, Cl, and S, which were calculated for the dominant reactions [K(n,p), Cl(n,p), and S(n,α)] using ENDF/B-VI or JENDL-3.2 cross sections and Q values. The whole brain kerma factors below 0.0253 eV were extrapolated down to 10^{-4} eV.

D. Kerma factors

Photon and neutron kerma factors are energy-dependent factors used to convert neutron or photon fluence spectra to kerma, which approximates absorbed dose.[40] The recently published H, ^{12}C, ^{14}N, ^{16}O, ^{31}P, and ^{40}Ca total isotopic neutron kermas in ICRU 63,[41] shown in Fig. 3 at their concentrations in an ICRU 46 adult brain,[7] are based on the ENDF/B-VI nuclear data library.[39] They were used to calculate kerma factors for the adult whole brain tissue composition specified in ICRU 46 (see Table I). Since kerma factors for the elements Na, S, Cl, and K included in the brain tissue composition are not reported in ICRU 63, neutron kerma factors for these elements were calculated from ENDF/B-VI or JENDL-3.2[42] cross section data and reaction Q values. However, because the contributions from Na and K represent a negligible fraction ($<0.1\%$) of the total neutron kerma for ICRU brain material at all neutron energies, the contributions from these two elements were neglected in the calculation of total neutron kerma. Kerma factors for the most significant neutron reactions for Cl and S, the (n,p) and (n,α) reactions, respectively, were calculated from JENDL-3.2 data because cross section data is not available in ENDF/B-VI for all of the stable isotopes of these two elements. Using the elemental cross sections and Q values to calculate kerma values for these reactions rather than by summing the kerma factors calculated for individual isotopes produced erroneous values and was therefore avoided; in the case of the $S(n,\alpha)$, the kerma factors below 2 MeV computed using the ENDF/B-VI natural S cross section were inflated by a factor of 2.

The neutron kerma factors that were used for clinical NCT treatment planning by the Harvard–MIT Program[35,43] are based on the kerma data of Caswell *et al.*,[44] derived from the ENDF/B-V data library. An earlier evaluation of neutron kerma data by Caswell *et al.*,[45] based on the ENDF/B-IV data library, was used to derive the neutron kerma factors for the various tissues reported in ICRU 46. The ICRU 63 report, in Sec. 6.4.2, states that for cross section evaluations earlier than ENDF/B-VI, ''energy deposition was not a primary concern...,'' and cross sections for several reactions were grouped together, which could ''...give significantly incorrect values for kerma coefficients.'' This possibility for significant discrepancy motivated a comparison of ICRU 46 neutron kermas for several tissue compositions with kerma factors computed for the same compositions from ICRU 63 elemental kerma factors. In addition, the differences in the kerma factors were evaluated for adult brain composition by comparing depth-kerma rate profiles computed with ICRU 46 or ICRU 63 based kerma factors. These calculations were performed for irradiation of the analytical representation of the modified Snyder head phantom with the generic epithermal neutron beam.

Another important issue related to neutron kerma is the treatment of neutrons below 0.0253 eV. In both ICRU 63 and

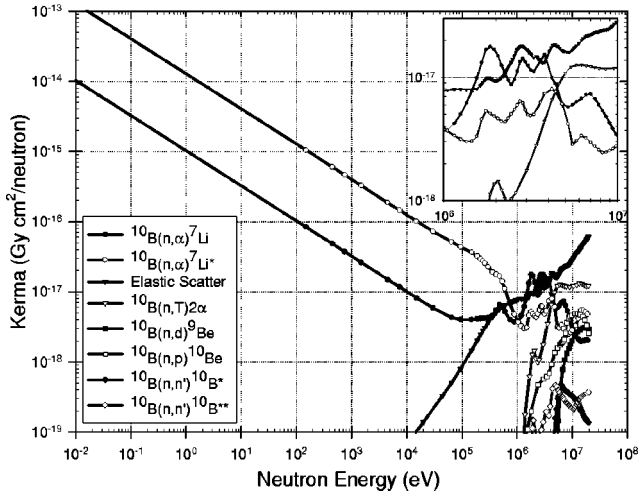

FIG. 4. Energy-dependent kerma factors for neutron reactions with ^{10}B, based on 1 μg/g ^{10}B. The two inelastic reactions [^{10}B$(n,n')^{10}$B* and ^{10}B$(n,n')^{10}$B**] are the two highest kerma-producing inelastic reactions below 10 MeV. Many more inelastic reactions of lesser importance are listed in the ENDF data, but are not shown in Fig. 4. The inset is an expansion of the 1–10 MeV region and shows only the first four reactions.

ICRU 46, the lowest reported neutron kerma data points are for 0.0253 eV. Since this energy only corresponds to the peak of the Maxwell–Boltzmann distribution at 20.5 °C, the contribution from neutrons below this energy is significant. Since nitrogen is the most significant contributor to the thermal neutron dose, and it is a $1/v$ absorber, the thermal neutron kerma values will increase as the neutron energy decreases, making the energy region below 0.0253 eV an important contributor to kerma. A reasonable treatment of neutron kerma below 0.0253 eV is log–log extrapolation of the kerma data points below 1 eV down to an energy where there are very few neutrons, such as 10^{-4} eV, as shown in Fig. 3. With the analytical model and the generic epithermal neutron beam, extrapolating the kerma down to 10^{-4} eV increased the thermal neutron doses throughout the phantom by 12% compared to the default treatment in MCNP, where all neutrons scored below the lowest energy point (0.0253 eV) are assigned the kerma value corresponding to the lowest energy point.

Photon kerma factors for ICRU brain tissue composition used in these calculations[46,47] are based on mass energy absorption coefficients (μ_{en}/ρ) calculated by Seltzer,[48] which update and expand the data from ICRU Report 46, which are derived from Hubbell's elemental data.[49] This most recent NIST evaluation of the photon kerma factors[46,47] was compared with ICRU 46 photon kerma factors by computing depth-kerma rate profiles in the analytical representation of the modified Snyder head phantom using monoenergetic photon beams of 0.2, 0.5, 1, 2, 5, and 10 MeV.

Kerma factors for ^{10}B were calculated from the energy-dependent cross sections and Q values from the ENDF/B-VI library[39] for the ^{10}B$(n,\alpha)^7$,Li and ^{10}B$(n,\alpha)^7$Li* reactions, which dominate at thermal energies. Figure 4 shows the ^{10}B kerma factors calculated for these two reactions as well as for several others, including the ^{10}B$(n,T)2\alpha$, elastic and inelastic scatter, ^{10}B$(n,\gamma)^{11}$B, ^{10}B$(n,p)^{10}$Be, and ^{10}B$(n,d)^9$Be reactions. Although these additional reactions do represent significant fractions of the total boron kerma at energies above several hundred keV, their impact on the total dose from ^{10}B is negligible due to the very low absolute value of the kerma factors in this energy range. To verify this, for both 1 MeV monoenergetic and epithermal neutron beams, depth-kerma rate profiles were calculated in the analytical representation of the modified Snyder head phantom using kerma factors derived from the ^{10}B(n,α) reactions only and using boron kerma factors that also include the two reactions most significant at high energies, elastic scatter, and the ^{10}B$(n,T)2\alpha$ reaction. The difference between the ^{10}B kerma rate profiles was smaller than the statistical uncertainty in the kerma rates (0.1%). For the boron depth-kerma rate profiles presented in the results, the kerma factors based only on the ^{10}B(n,α) reactions were used.

The kerma factors for boron and the tissue kerma factors derived from the ICRU 63 data and JENDL-3.2 data are available in the EPAPS electronic database.[60]

E. Thermal neutron scattering treatment

At neutron energies below several eV, the motion of a target nucleus and its chemical binding state are important factors in neutron scattering.[13] At these low energies, the neutron energy is comparable to the thermal energy of the target atom as well as to its chemical binding energy. Hence, the thermal motion of the target atom alters the effective scattering cross section as well as energy transfer to or from the incident neutron. In collisions with bound nuclei or nuclei in condensed matter, the binding or presence of nearby atoms may affect the recoil of the target nucleus and thus influence the energy and angle of the outgoing neutron. The default treatment for thermal neutron scattering in MCNP is the free gas thermal treatment, which, as the name implies, neglects the complex chemical binding effects and interaction of the target atom with other nearby atoms, but does include thermal motion of the target nucleus in the scattering kinematics.[24] For a few select molecules and solids, the $S(\alpha,\beta)$ thermal neutron scattering treatment, a complete representation of the thermal neutron scattering law, is available in MCNP. To account for the molecular binding effects of hydrogen in the biological materials of these calculations, the $S(\alpha,\beta)$ thermal scattering treatment for hydrogen in light water at 300 K was generally used. The effect of the different thermal neutron scattering treatments on dose rates was evaluated by comparing dose-depth profiles calculated using the free gas thermal treatment or $S(\alpha,\beta)$ thermal scattering treatment in the analytical model with the "generic" epithermal neutron beam.

F. Neutron and photon source beams

The reference calculations were performed using individual monoenergetic and monodirectional beams of 0.0253 eV, 1, 2, 10, 100, and 1000 keV neutrons and 0.2, 0.5, 1, 2, 5, and 10 MeV photons. These calculations were run to high statistical convergence, with statistical uncertainty of less

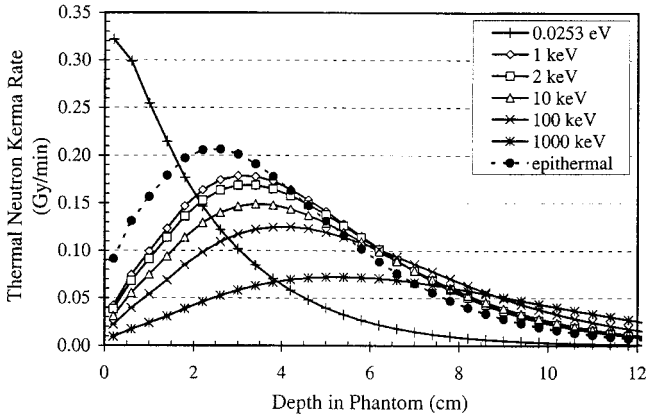

FIG. 5. Thermal neutron depth-kerma rate profiles calculated in the analytical representation of the modified Snyder head phantom for various neutron beams.

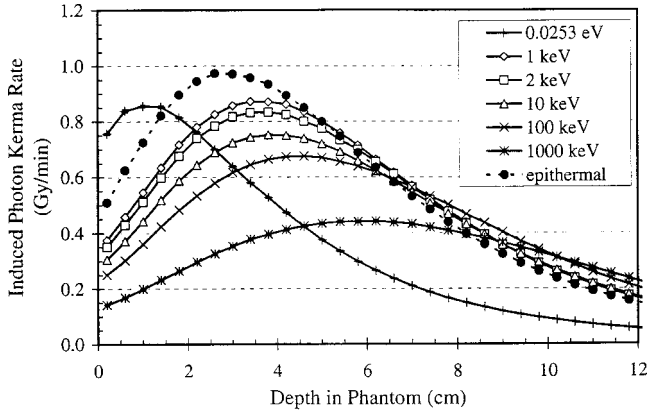

FIG. 7. Induced photon depth-kerma rate profiles calculated in the analytical representation of the modified Snyder head phantom for various neutron beams.

than 1% in the center of the model for each dose component. All calculations were run for at least 50 million particle histories. In addition to these monoenergetic beams, a generic epithermal neutron beam with 1% fast neutron flux contamination (10 keV to 2 MeV) and 10% thermal flux contamination (1 meV to 0.5 eV), similar to those proposed for use in clinical BNCT, was also employed. Inside each of the three energy bins of this epithermal spectrum, the modeled neutron spectrum approximated a $1/E$ distribution.[13] All beams were 10 cm in diameter and were sampled uniformly in area; i.e., radius, r, was sampled from the distribution $f(r)=(2/R^2)r$, where R is the maximum radius, 5 cm. The intensities of these beams were normalized to a neutron or photon flux of 10^{10} particles/cm^2 s. For the generic epithermal neutron beam, source biasing was used to sample the higher-energy portion of the neutron spectrum more frequently and thereby reduce the statistical uncertainty of the fast neutron dose deep in the phantom.

III. RESULTS

In this paper we present the results from a number of different computational dosimetry studies relating to neutron capture therapy. Most importantly, reference depth-kerma rate profiles, for comparing and verifying NCT treatment planning codes, are presented in Sec. III A. These profiles, based on an analytical model of the modified Snyder head phantom, are then compared to voxel models of the same phantom in Sec. III B to examine the effect of voxel size. In Sec. III C, differences in kerma rates arising from variation in the tissue nitrogen concentration are presented. In Sec. III D, we examine the effects of changing kerma data from ICRU 46 (based on ENDF/B-IV) to ICRU 63 for neutrons (based on ENDF/B-VI) and to the most recent NIST evaluation for photons. In Sec. III E, the impact of using two different thermal neutron scattering treatments is analyzed.

A. Reference dosimetry calculations

Figures 5–8 show the reference thermal neutron, fast neutron, induced photon, and boron depth-kerma rate profiles calculated for irradiation of the analytical model of the modified Snyder head phantom with the monodirectional, monoenergetic neutron beams of 0.0253 eV, 1, 2, 10, 100, and 1000 keV, and the epithermal neutron beam. Presentation of the depth-kerma rate profiles for the 8 mm voxel model is

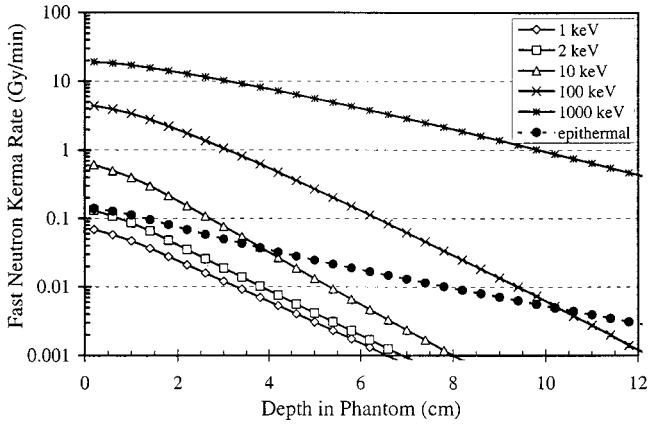

FIG. 6. Fast neutron depth-kerma rate profiles calculated in the analytical representation of the modified Snyder head phantom for various neutron beams.

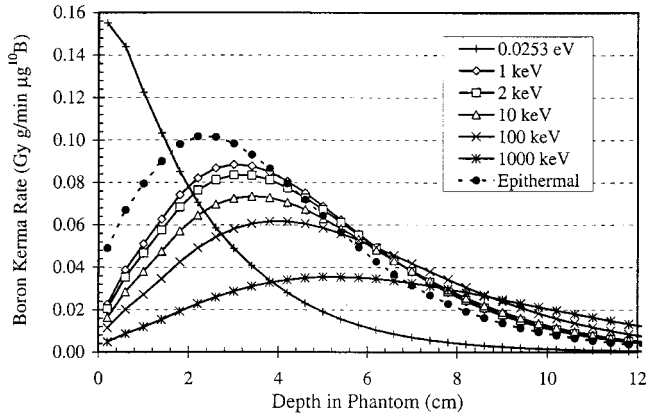

FIG. 8. Boron depth-kerma rate profiles for tissue concentrations of 1 μg/g ^{10}B calculated in the analytical representation of the modified Snyder head phantom for various neutron beams.

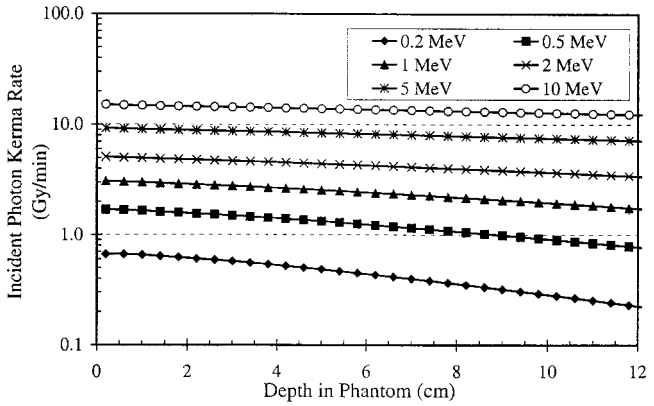

FIG. 9. Incident photon depth-kerma rate profiles calculated in the analytical representation of the modified Snyder head phantom for various monoenergetic photon beams.

omitted for brevity since these data are also available electronically. Figure 9 shows the incident photon depth-kerma rate distribution for irradiation of the same model with the monoenergetic photon beams of 0.2, 0.5, 1, 2, 5, and 10 MeV. The statistical uncertainty (1 σ) for each point in Figs. 5–9 is smaller than the sizes of the data points. These figures show a number of interesting effects. As expected, increasing the neutron beam energy increases the fast neutron kerma rate by several orders of magnitude, and produces differences in the peak thermal neutron and induced photon kerma rates of as much as a factor of 3. At the surface of the phantom, the fast neutron kerma rate increases by two orders of magnitude and even more at depth in the phantom, as the neutron energy increases from 1 keV to 1 MeV. As the neutron beam energy increases, both the thermal neutron kerma rate and induced photon kerma rate peaks move deeper into the phantom and broaden significantly. Increasing the energy of the incident photon beam from 0.2 to 10 MeV likewise increases the peak photon kerma rate by a factor of 20.

B. Voxel models

Depth-kerma rate profiles calculated for the generic epithermal beam in voxel model representations of the modified Snyder head phantom with 16, 8, and 4 mm voxels, and in the analytical representation of the head phantom are shown in Figs. 10–12 along with their respective differences from the analytical model results. The model with the smallest voxel size, 4 mm, shows the best agreement with the analytical model for all dose components, typically differing by less than 2%. The 8 mm voxel model kerma rates are within 3%–5% of the analytical model kerma rates for all depths and are usually lower than the analytical model kerma rates. However, the 16 mm voxel model produced unacceptably large discrepancies (maximum deviations of 13%) for all dose components.

C. Tissue compositions

Since kerma factors are the sum of the products of the isotopic cross sections and the energy imparted to charged

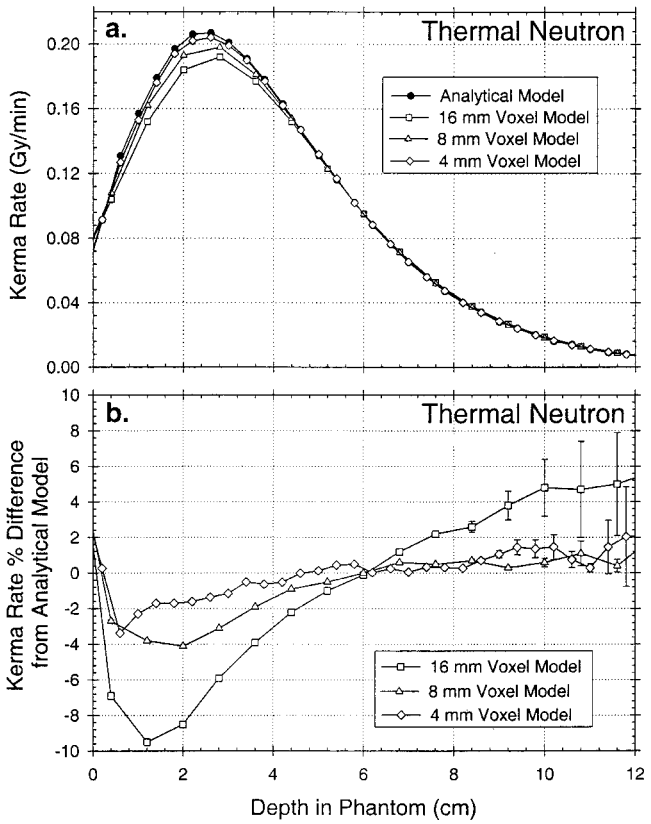

FIG. 10. Effect of voxel size on thermal neutron depth-kerma rate profiles. (a) Profiles for the analytical and 4, 8, and 16 mm voxel models of the modified Snyder head phantom calculated for an epithermal neutron beam. (b) Percentage differences in thermal neutron kerma rates between voxel models and the analytical model.

particles weighted by the mass fraction in tissue for each isotope, they will vary with the assumed tissue compositions used to derive the kerma factors. As stated in ICRU Report 46, ''Uncertainties in the absorbed-dose estimations in body tissues arise both from uncertainties in the composition of the tissues and from uncertainties in the radiation interaction coefficients. The former are usually larger.'' Of particular interest, due to its large effect on the total brain kerma and variability among people, is the concentration of nitrogen. The kerma factors for adult brain based on two different nitrogen concentrations, 2.2%[7] and 1.84%[50] by mass, a 16.4% difference, are plotted in Fig. 13. Correspondingly, the thermal neutron kerma factor for adult brain containing 2.2% by mass ^{14}N is 15.8% higher. Small changes in the tissue ^{14}N concentration perturb neutron transport very little. Above ~1 keV, the total brain kerma for the composition with 1.84% nitrogen is higher than for a nitrogen concentration of 2.2% because all of the other elements were uniformly increased in concentration to maintain constant density.

Neutron kerma factors computed for brain, cranium, and skin using ICRU 63 elemental data (based on ENDF/B-VI) and the S(n,α) and Cl(n,p) cross section and Q value data from JENDL-3.2 are shown in Fig. 14(a). Below 30 eV, the difference between the kerma factors for cranium and skin is about 5% because their nitrogen concentrations are 5% dif-

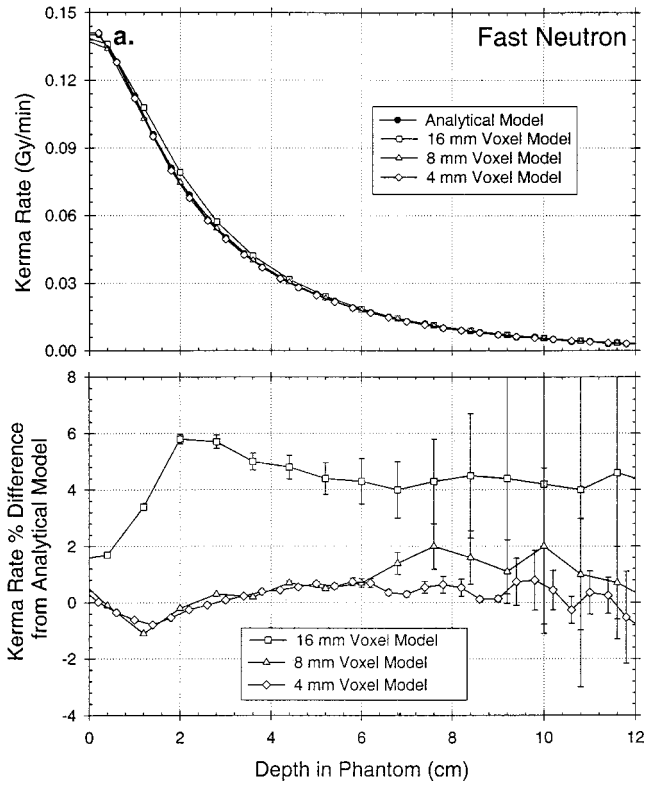

FIG. 11. Effect of voxel size on fast neutron kerma rate profiles. (a) Profiles for the analytical and 4, 8, and 16 mm voxel models of the modified Snyder head phantom calculated for an epithermal neutron beam. (b) Percentage differences in fast neutron kerma rates between the voxel models and the analytical model.

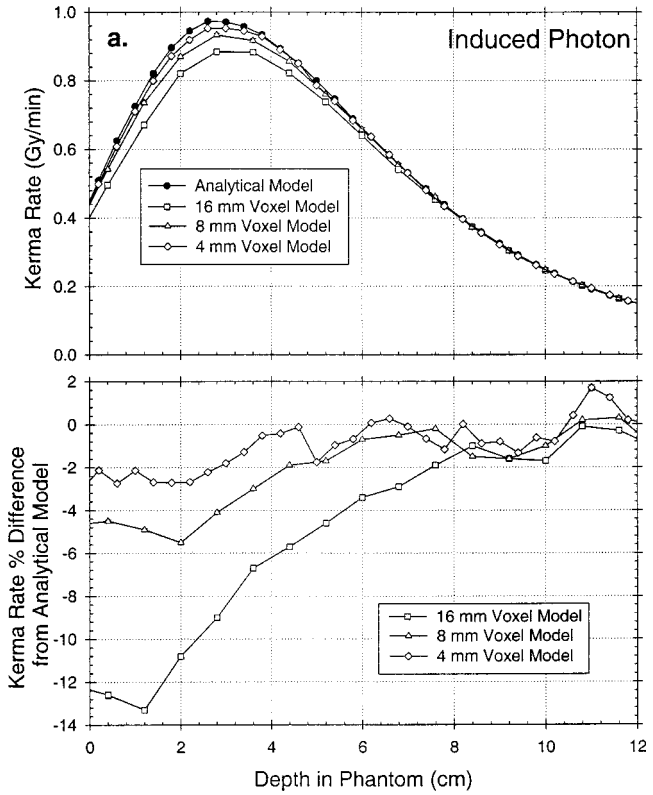

FIG. 12. Effect of voxel size on the induced photon kerma rate profile. (a) Profiles for the analytical and 4, 8, and 16 mm voxel models of the modified Snyder head phantom calculated for an epithermal neutron beam. (b) Percentage differences in induced photon kerma rates between voxel models and the analytical model.

ferent, as shown in Table I. The skin and brain kerma factors above 200 eV differ by only 6% or less due to corresponding differences in their hydrogen concentrations.

D. Kerma factors

The ICRU 63 elemental kerma data were used to compute updated tissue kerma factors and these were compared to ICRU 46 tissue kerma data. The differences between brain, cranium, and skin neutron kerma factors computed from ICRU 63 data (based on ENDF/B-VI) and the S(n,α) and Cl(n,p) data from JENDL-3.2 and those available in ICRU 46 (based on ENDF/B-IV), shown in Fig. 14(b), are generally less than 2%. Large differences between the two sets of kerma factors are evident around 398 eV due to the inclusion of a resonance peak of the chlorine (n,p) reaction, but this peak is only a few eV in width. In the epithermal energy region, where the neutron kerma is at its minimum, however, the ICRU 63 based adult whole brain kerma is 1%–2% higher than ICRU 46, possibly due to the inclusion of the S(n,α) reaction. When the S(n,α) reaction is excluded, that difference falls to less than 0.5%. With an epithermal neutron beam, however, using the ICRU 63 kerma factors produced thermal neutron depth-kerma rate profiles less than 2% lower than those calculated with ICRU 46 kerma factors, as shown in Fig. 15.

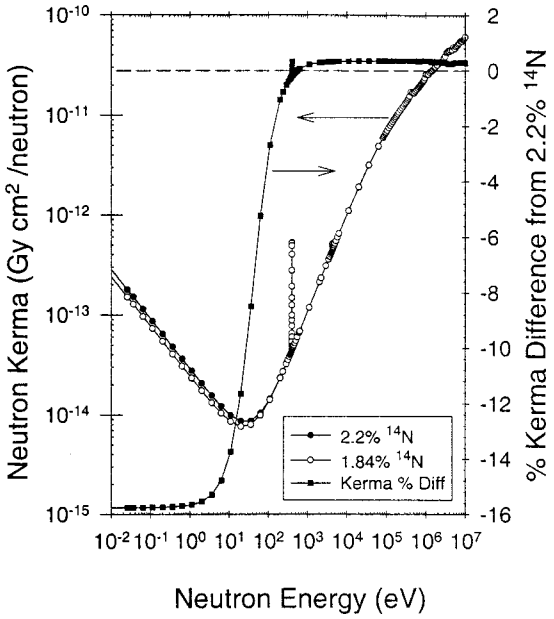

FIG. 13. Energy dependent neutron kerma factors computed using ICRU 63 elemental kerma data and data from JENDL-3.2 for adult whole brain compositions with nitrogen concentrations of 2.2% (Ref. 7) and 1.84% (Ref. 50) by mass. The difference between the two sets of kerma factors decreases from 15.8% at thermal energies to negligible differences at energies above 1 keV.

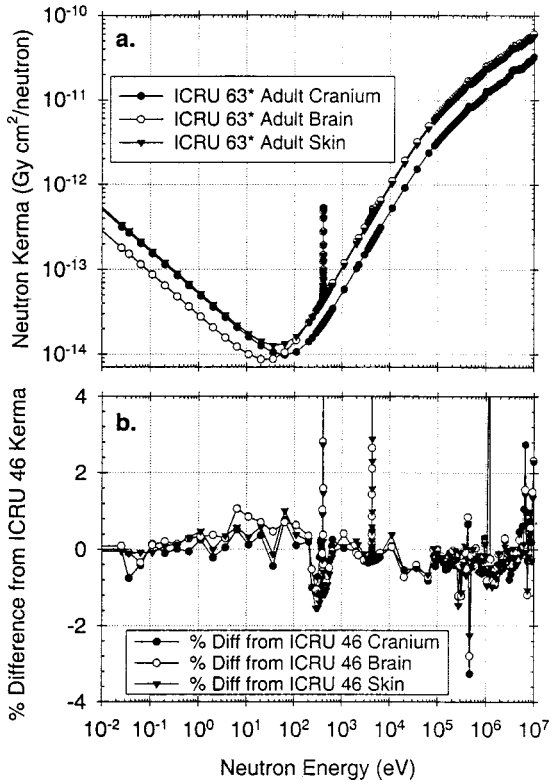

FIG. 14. (a) Neutron kerma factors for adult cranium, brain, and skin composition based on ICRU 63 and JENDL-3.2 data, and (b) their differences from ICRU 46 neutron kerma factors.

The most recent NIST evaluation of photon kerma factors[46,47] (used in these calculations) for ICRU brain composition were compared with ICRU 46 kerma factors for the same composition by computing depth-kerma rate profiles for irradiation of the analytical representation of the modified

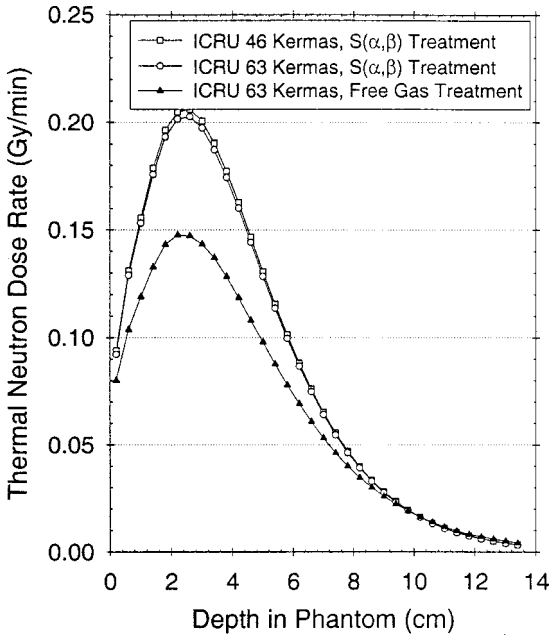

FIG. 15. The effects of different kerma factors and thermal neutron scattering treatments on thermal neutron kerma rates.

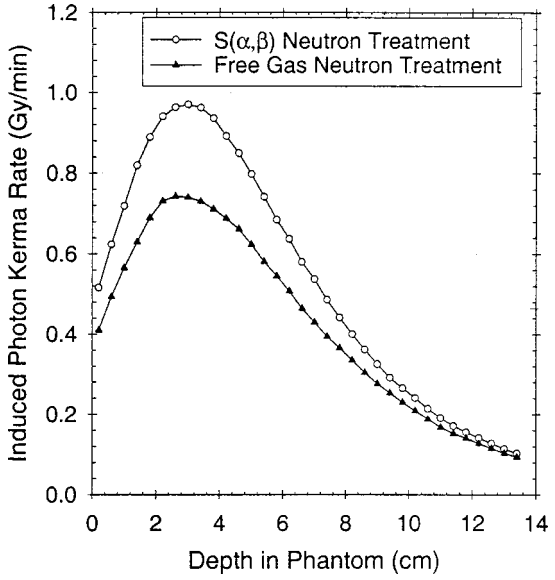

FIG. 16. A comparison of induced photon kerma rates computed with the S(α, β) and free gas thermal neutron scattering treatments.

Snyder head phantom with monoenergetic photon beams of 0.2, 0.5, 1, 2, 5, and 10 MeV using both sets of kerma factors. The two kerma sets produced no significant differences in these calculations. Differences in photon kerma rate profiles were less than the statistical uncertainty in the difference between the profiles, which was 0.2%.

E. Thermal neutron scattering treatment

Differences between the free gas treatment and the S(α,β) thermal neutron scattering treatment for hydrogen in water produced significant differences in neutron transport that, at most depths, resulted in increased dose rates for those components derived from the thermal neutron flux. The maximum thermal neutron dose rate calculated using the S(α,β) thermal neutron scattering treatment was 37% higher than that calculated using the free gas treatment, as indicated in Fig. 15. In addition, the location of the peak dose rates differed slightly, by ~0.4 cm. This difference, however, decreases with depth so that by ~10 cm depth, the thermal neutron kerma rates are equal. Deeper than ~10 cm, the S(α,β) treatment produces thermal neutron kerma rates slightly lower than the free-gas treatment. Since both the ^{10}B and neutron kerma factors follow a $1/v$ relationship in the thermal region, similar behavior should be expected for ^{10}B dose rate profiles. The effect on induced photon kerma rates, shown in Fig. 16, was similar, with the S(α,β) treatment producing a maximum kerma rate 30% higher than with the free gas treatment. The locations of the maxima also differed slightly, by ~0.4 cm. However, the induced photon kerma rate calculated with the S(α,β) treatment was higher than that calculated using the free gas treatment at all depths. Since the scattering cross sections differ below ~4 eV, there is a slight effect on the fast neutron dose rates, such that S(α,β) treatment produced 0.5% higher fast neutron dose rates.

IV. DISCUSSION

In this paper we present a set of reference dosimetry calculations for neutron capture therapy using the modified Snyder head phantom and monodirectional beams of neutrons and photons. Depth-kerma rate profiles were calculated for monoenergetic neutron and photon beams spanning the realistic energy ranges of existing and future epithermal neutron beams as well as for a ''generic'' broad spectrum epithermal neutron beam. The depth-kerma rate profiles reported here for the modified Snyder head phantom will be useful for evaluating NCT treatment planning software packages by comparing their results to these reference calculations. The broad spectrum epithermal neutron beam may be expected to yield a more realistic estimate of the impact on dose resulting from the variations in input parameters. The monoenergetic beam data, however, may be more useful for elucidating the causes of differences between or errors in treatment planning systems, such as a particular aspect of transport physics.

In addition to the reference calculations, in this study we examined the effects of several modeling parameters, including voxel model representation and voxel size, composition, kerma data, and thermal neutron scattering treatments on transport and dosimetry calculations. For the broad spectrum epithermal neutron beam, differences in material compositions, kerma data, and free gas or the S(α,β) thermal neutron scattering treatment for hydrogen in water resulted in differences in the thermal neutron depth-kerma rate profiles of 16%, 2%, and 37%, respectively. The impact of some of these modeling parameters is significantly larger than the 4% difference between the analytical model and the 8 mm voxel model, indicating that modeling considerations such as composition and the thermal neutron scattering law can have a larger impact than voxel size.

The calculations presented here are kerma rate profiles. For all of the dose components except photons, the dose is well approximated by kerma. The neutron reactions with nitrogen and hydrogen, which comprise most of the thermal and fast neutron kerma, produce short-range charged particles, such that their kinetic energy is absorbed locally, i.e., well within 100 μm of the reaction site. The same is true for the boron dose component. Photons produce energetic electrons with ranges comparable to the voxel sizes considered here, e.g., for a 1 MeV electron, the range in tissue is $\sim$4 mm. Hence, for photons, charged particle equilibrium does not always hold true and kerma does not always approximate the dose well, particularly with the incident photon beams considered here. As anticipated, the kerma rate profiles shown in Fig. 9 do not exhibit buildup at shallow depths, as would be expected for the dose.

The thermal neutron kerma factors are also approximate, since they are the sums of elemental or isotopic kerma factors, which neglect molecular effects. Since the thermal neutron scattering law had a significant effect on the neutron transport, a significant impact on the kerma factors might also be expected at low energies. These effects arise from differences in neutron cross sections and energy transfer due to chemical binding. According to Caswell, kerma values below $\sim$30 eV could be affected.[44] Several authors, including those of ICRU 63,[37,41] acknowledge the problem and, although they report elemental kerma factors down to 0.0253 eV, they do not report material kerma factors for neutron energies below 11 eV. In the case of kerma factors for brain, however, the low-energy kerma is dominated by the ^{14}N(n,p)^{14}C reaction, a reaction that should be affected minimally by molecular effects, due to the high Q value of the reaction. Since the thermal neutron dose is an important contribution to the total dose in many neutron therapies, its calculation, even if approximate, is important.

TABLE II. Computer resources used in epithermal neutron beam simulations. Simulations were carried out using a 400 MHz Pentium II computer.

Model	Memory required (Mbytes)	Time to complete 50 million histories (hours)
Analytical	7.2	30.1
16 mm	13.9	28.6
8 mm	44.1	41.2
4 mm	272.7	143.0

Throughout this paper, the results from the 16 mm voxel model simulations have been described as unacceptable, even though the agreement with the depth-kerma rate profiles of the analytical model indicates maximum differences of only 9.5%, 5.8%, and 13.3% for thermal neutron, fast neutron, and induced photon dose components, respectively (see Figs. 10–12). The improvement of the 4 mm voxel model over the 8 mm voxel model, as measured by deviation from the analytical model depth-kerma rate profiles, was small. Since little additional accuracy is gained from using 4 mm voxels, it is probably not worth the increased additional computational resources (memory and time; see Table II) needed to run the much more memory intensive 4 mm voxel model, unless a very accurate calculation of the surface dose is required. However, using a modified version of MCNP with a more efficient (both in terms of computational speed and memory) lattice representation of the geometry, rather than representing each voxel with a cell, the required computational resources can be reduced for all voxel sizes.[51,52] A further reduction in the size of voxels, even down to SERA's ''univels'' [53] is not expected to significantly improve the accuracy of the Snyder head phantom voxel models, since the 4 mm voxel model produces results already very close to the analytical version. [Univels (uniform volume elements) form the basis of the tracking algorithm in SERA.[53] In SERA, each univel corresponds to a single image pixel.] However, the use of univels may improve the accuracy of a patient models in regions of high heterogeneity, such as the sinus cavities.

These data are presented as a set of reference calculations. Although they are not compared to experimental measurements, we have a high degree of confidence in these results since MCNP has been extensively benchmarked and verified,[54] and has been compared to experiments in a wide variety of circumstances.[55,56] For a similar NCT problem, the

irradiation of a water-filled head phantom with the MIT fission converter neutron beam, MCNP depth-dose profiles agreed well with measurements.[57,58]

MCNP has also been compared to other computer programs in similar NCT calculations. MCNP produced gamma, thermal neutron, and fast neutron doses within 2% of those calculated with rtt_MC, the Monte Carlo engine in BNCT_rtpe,[21] for some simplistic geometrical phantoms.[23] Comparisons using models constructed from patient CT image data have also produced similar agreement. Dose distributions and dose–volume histograms calculated with MacNCTPlan (which uses MCNP as the dose calculation engine) and BNCT_rtpe were in very close agreement.[23] As part of a demonstration of rapid treatment planning calculations using deterministic transport methods, MCNP was compared to TORT,[59] a three-dimensional discrete ordinates code, and ^{10}B, neutron, and photon doses for more than 95% of all cells were found to agree to within 5%.[15]

V. CONCLUSIONS

Depth-kerma rate curves were calculated for irradiation of the modified Snyder head phantom with monoenergetic and broad-spectrum epithermal neutron and monoenergetic photon beams using the radiation transport code MCNP4B. The test problems reported here may be used as reference data for the verification and intercomparison of NCT treatment planning software. Additional analyses investigated the impact of several modeling issues relevant to NCT treatment planning and dosimetry calculations. Using a voxel model was found to be accurate in representing the phantom geometry when small (<1 cm) voxels were used. However, for large (16 mm) voxels, deviations in kerma rates were unacceptably large. The thermal neutron scattering law, nitrogen concentration of the tissue used in deriving the kerma factors, and the presence of explicitly modeled ^{10}B in the phantom were found to produce significant ($>10\%$) differences in thermal neutron kerma rate profiles. Updating kerma factors to use the most recent data produced only small ($<2\%$) differences in kerma rates. These calculations will be available electronically in the EPAPS database as an aid in the verification of existing and new NCT treatment planning software.[60]

ACKNOWLEDGMENTS

This research was supported by Grant No. 11066 from the International Atomic Energy Agency and by Grant No. DE-FG02-97ER62193 from the U.S. Department of Energy. The authors would also like to thank the Harvard–MIT BNCT team, especially Dr. Matthew Palmer, Mr. Gustavo Santa Cruz, and Dr. Paul Busse.

[a]Electronic mail: wskiger@mit.edu

[1] R. Zamenhof, P. Busse, O. Harling, and T. Goorley, ''Boron neutron capture therapy,'' in *The Modern Technology of Radiation Oncology: A Compendium for Medical Physicists and Radiation Oncologists*, edited by J. Van Dyk (Medical Physics Publishing, Madison, WI, 1999), pp. 981–1020.

[2] J. C. Yanch, R. E. Shefer, and P. M. Busse, ''Boron neutron capture therapy,'' Sci. Med. **6**, 18–27 (1999).

[3] R. F. Barth, A. H. Soloway, J. H. Goodman, R. A. Gahbauer, N. Gupta, T. E. Blue, W. Yang, and W. Tjarks, ''Boron neutron capture therapy of brain tumors: An emerging therapeutic modality,'' Neurosurgery **44**, 433–450 (1999).

[4] ''Chart of the nuclides,'' Version 14, Knolls Atomic Power Laboratory, San Jose, CA, 1988.

[5] J. A. Coderre and G. M. Morris, ''The radiation biology of boron neutron capture therapy,'' Radiat. Res. **151**, 1–18 (1999).

[6] A. H. Soloway, W. Tjarks, B. A. Barnum, F.-G. Rong, R. F. Barth, I. M. Codogni, and J. G. Wilson, ''The chemistry of neutron capture therapy,'' Chem. Rev. **98**, 1515–1562 (1998).

[7] ICRU 46, ''Photon, electron, proton, and neutron interaction data for body tissues,'' International Commission on Radiation Units and Measurements, Bethesda, MD, 1992.

[8] J. A. Coderre, M. S. Makar, P. L. Micca, M. M. Nawrocky, H. B. Liu, D. D. Joel, D. N. Slatkin, and H. I. Amols, ''Derivations of relative biological effectiveness for the high-let radiations produced during boron neutron capture irradiations of the 9L rat gliosarcoma *in vitro* and *in vivo*,'' Int. J. Radiat. Oncol. Biol. Phys. **27**, 1121–1129 (1993).

[9] G. M. Morris, J. A. Coderre, P. L. Micca, C. D. Fisher, J. Capala, and J. W. Hopewell, ''Central nervous system tolerance to boron neutron capture therapy with p-boronophenylalanine,'' Br. J. Cancer **76**, 1623–1629 (1997).

[10] W. S. Kiger III, M. R. Palmer, R. G. Zamenhof, and P. M. Busse, ''A pharmacokinetic model for the concentration of boron-10 in blood following BPA-f administration in humans,'' in *Frontiers in Neutron Capture Therapy*, edited by F. M. Hawthorne, K. Shelley, and R. J. Wiersema (Kluwer Academic/Plenum, New York, 2001), pp. 249–256.

[11] W. S. Kiger III, M. R. Palmer, K. J. Riley, R. G. Zamenhof, and P. M. Busse, ''A pharmacokinetic model for the concentration of ^{10}B in blood after boronophenylalanine–fructose administration in humans,'' Radiat. Res. **155**, 611–618 (2001).

[12] F. M. Khan, *The Physics of Radiation Therapy* (Williams & Wilkins, Baltimore 1984).

[13] J. J. Duderstadt and L. J. Hamilton, *Nuclear Reactor Analysis* (Wiley, New York, 1976).

[14] D. W. Nigg, P. D. Randolph, and F. J. Wheeler, ''Demonstration of three-dimensional deterministic radiation transport theory dose distribution analysis for boron neutron capture therapy,'' Med. Phys. **18**, 43–53 (1991).

[15] D. T. Ingersoll, C. O. Slater, E. L. Redmond II, and R. G. Zamenhof, ''Comparison of TORT and MCNP dose calculations for BNCT treatment planning,'' in *Advances in Neutron Capture Therapy*, edited by B. Larsson, J. Crawford, and R. Weinreich (Elsevier, Amsterdam, 1997), Vol. I, pp. 95–99.

[16] C. P. Raaijmakers, I. A. Bruinvis, E. L. Nottelman, and B. J. Mijnheer, ''A fast and accurate treatment planning method for boron neutron capture therapy,'' Radiother. Oncol. **46**, 321–332 (1998).

[17] R. Zamenhof, E. Redmond II, G. Solares, D. Katz, K. Riley, S. Kiger, and O. Harling, ''Monte Carlo-based treatment planning for boron neutron capture therapy using custom designed models automatically generated from CT data,'' Int. J. Radiat. Oncol. Biol. Phys. **35**, 383–397 (1996).

[18] W. S. Kiger III, R. G. Zamenhof, G. R. Solares, E. L. Redmond II, and C.-S. Yam, ''MacNCTPlan. An improved Macintosh based BNCT treatment planning program,'' Trans. Am. Nucl. Soc. **75**, 38–39 (1996).

[19] R. G. Zamenhof, G. R. Solares, W. S. Kiger III, E. L. Redmond II, P. M. Busse, and C. S. Yam, ''MacNCTPlan: An improved Macintosh-based treatment planning program for boron neutron capture therapy,'' in *Advances in Neutron, Capture Therapy*, edited by B. Larsson, J. Crawford, and R. Weinreich (Elsevier, Amsterdam, 1997), pp. 100–105.

[20] D. W. Nigg, ''Methods for radiation dose distribution analysis and treatment planning in boron neutron capture therapy,'' Int. J. Radiat. Oncol., Biol. Phys. **28**, 1121–1134.

[21] D. W. Nigg, F. J. Wheeler, D. E. Wessol, J. Capala, and M. Chadha, ''Computational dosimetry and treatment planning for boron neutron capture therapy,'' J. Neuro-Oncol. **33**, 93–104 (1997).

[22] D. E. Wessol, C. A. Wemple, F. J. Wheeler, M. T. Cohen, M. B. Rossmeier, and J. Cogliati, ''SERA: Simulation Environment for Radiotherapy Applications User's Manual Version 1B0,'' http://esus.cs.montana.edu/~bnct/manual/toc.html, Department of Computer Science, Montana State University, 1999.

[23] T. Goorley, J. Capala, F. Wheeler, W. S. Kiger III, R. Zamenhof, M. R. Palmer, and D. Nigg, ''A comparison of two treatment planning pro-

grams: BNCT-RTPE and MacNCTPlan,'' in Ref. 10, pp. 207–212.
[24] J. F. Briesmeister, ''MCNP—A general Monte Carlo N-particle transport code,'' LA12625-M, Version 4B, Los Alamos National Laboratory, 1997.
[25] J. R. Albritton, ''Analysis of the SERA treatment planning system and its use in boron neutron capture synovectomy,'' M. S. thesis, Massachusetts Institute of Technology, 2001.
[26] S. A. Wallace, B. J. Allen, and J. N. Mathur, ''Monte Carlo neuton photon treatment planning calculations: Modeling from CT scans with variable voxel size,'' in *Cancer Neutron Capture Therapy*, edited by Y. Mishima (Plenum, New York, 1996), pp. 295–302.
[27] N. Cerullo and G. Daquino, '' 'CARONTE,' A treatment planning system based on real boron distribution and MCNP-4A code: Result and discussion,'' in Ref. 10, pp. 225–230.
[28] H. Kumada, K. Yamamoto, Y. Torii, A. Matsumura, T. Yamamoto, and Y. Nakagawa, ''Development of the patient setting system for BNCT at JRR-4,'' in *Proceedings of the 9th International Symposium on Neutron Capture Therapy for Cancer*, Osaka, Japan, 2000, pp. 281–282.
[29] K. J. Riley, P. J. Binns, and O. K. Harling, ''A physical dosimetry intercomparison for BNCT,'' Massachusetts Institute of Technology Nuclear Reactor Laboratory, Cambridge, MA, 2001.
[30] F. Stecher-Rasmussen, I. Auterinen, A. Beddoe, I. Goncalves, H. Järvinen, A. Kosunen, B. Larsson, M. Marek, B. Mijnheer, C. P. J. Raaijmakers, S. Savolainen, W. P. Voorbank, P. Watkins, and E. Zsolnay, ''A code of practice for the dosimetry of BNCT in Europe,'' in Ref. 15, pp. 237–240.
[31] O. K. Harling (private communication, 2000).
[32] W. S. Snyder, M. R. Ford, G. G. Warner, and H. L. Fisher, Jr., ''Estimates for absorbed fractions for monoenergetic photon sources uniformly distributed in various organs of a heterogeneous phantom,'' J. Nucl. Med. Suppl. **3**, 47 (1969).
[33] R. D. Rogus, O. K. Harling, and J. C. Yanch, ''Mixed field dosimetry of epithermal neutron beams for boron neutron capture therapy at the MITR-II research reactor,'' Med. Phys. **21**, 1611–1625 (1994).
[34] O. K. Harling, K. A. Roberts, D. J. Moulin, and R. D. Rogus, ''Head phantoms for neutron capture therapy,'' Med. Phys. **22**, 579–583 (1995).
[35] R. G. Zamenhof, S. D. Clement, O. K. Harling, J. F. Brenner, D. E. Wazer, H. Madoc-Jones, and J. C. Yanch, ''Monte Carlo based dosimetry and treatment planning for neutron capture therapy of brain tumors,'' in *Neutron Beam Design, Development and Performance for Neutron Capture Therapy*, edited by O. K. Harling, R. G. Zamenhof, and J. A. Bernard (Plenum, New York, 1990), pp. 283–305.
[36] ICRU 44, ''Tissue substitutes in radiation dosimetry and measurement,'' International Commission on Radiation Units and Measurements, Bethesda, MD, 1989.
[37] M. Chadwick, H. Barschall, R. Caswell, P. DeLuca, G. Hale, D. Jones, R. MacFarlane, J. Meulders, H. Schuhmacher, U. Schrewe, A. Wambersie, and P. Young, ''A consistent set of neutron kerma coefficients from thermal to 150 MeV for biologically important materials,'' Med. Phys. **26**, 974–991 (1999).
[38] J. S. Hendricks, S. C. Frankle, and J. D. Court, ''ENDF/B-VI data for MCNP,'' LA-12891, Los Alamos National Laboratory, December 1994.
[39] Cross Section Evaluation Working Group, ''ENDF/B-VI summary documentation,'' BNL-NCS-17541, National Nuclear Data Center, Brookhaven National Laboratory, Upton, NY, 1991.
[40] A. B. Chilton, J. K. Shultis, and R. E. Faw, *Principles of Radiation Shielding* (Prentice–Hall, Englewood Cliffs, 1984).
[41] ICRU 63, ''Nuclear data for neutron and proton radiotherapy and for radiation protection,'' International Commission on Radiation Units and Measurements, Bethesda, MD, 2000.
[42] T. Nakagawa, K. Shibata, S. Chiba, T. Fukahori, Y. Nakajima, Y. Kikuchi, T. Kawano, Y. Kanda, T. Ohsawa, H. Matsunobu, M. Kawai, A. Zukeran, T. Watanabe, S. Igarasi, K. Kosako, and T. Asami, ''Japanese evaluated nuclear data library version 3 revision 2: JENDL-3.2,'' J. Nucl. Sci. Technol. **32**, 1259 (1995).
[43] M. R. Palmer, J. T. Goorley, W. S. Kiger III, P. M. Busse, and R. G. Zamenhof, ''Treatment planning and dosimetry for the Harvard–MIT phase-I clinical trial for Cranial BNCT,'' in Ref. 28, pp. 147–148.
[44] R. S. Caswell, J. J. Coyne, and M. L. Randolph, ''Kerma factors of elements and compounds for neutron energies below 30 MeV,'' Int. J. Appl. Radiat. Isot. **33**, 1227–1262 (1982).
[45] R. S. Caswell, J. J. Coyne, and M. L. Randolph, ''Kerma factors for neutron energies below 30 MeV,'' Radiat. Res. **83**, 217–254 (1980).
[46] J. H. Hubbell and S. M. Seltzer, ''Tables of x-ray mass attenuation coefficients and mass energy–absorption coefficients 1 keV to 20 MeV for elements $Z=1$ to 92 and 48 additional substances of dosimetric interest,'' NISTIR 5632, National Institute of Standards and Technology, Gaithersburg, MD, May 1995.
[47] J. H. Hubbell and S. M. Seltzer, ''Tables of x-ray mass attenuation coefficients and mass energy–absorption coefficients,'' http:/physics.nist.gov/xaamdi, National Institute of Standards and Technology, Gaithersburg, MD, 1997.
[48] S. Seltzer, ''Calculation of photon mass energy-transfer and mass energy-absorption coefficients,'' Radiat. Res. **136**, 147–170 (1993).
[49] J. Hubbell, ''Photon mass attenuation and energy-absorption coefficients from 1 keV to 20 MeV,'' Int. J. Appl. Radiat. Isot. **33**, 1269–1290 (1982).
[50] R. A. Brooks, G. DiChiro, and M. R. Keller, ''Explanation of cerebral white–grey contrast in computed tomography,'' J. Comput. Tomogr **4**, 489 (1980).
[51] J. T. Goorley, ''Boron neutron capture therapy treatment planning improvements,'' M. S. thesis, Massachusetts Institute of Technology, 1998.
[52] J. T. Goorley, G. McKinney, K. Adams, and G. Estes, ''MCNP enhancements, parallel computing and error analysis for BNCT,'' in Ref. 10, pp. 599–604.
[53] M. W. Frandsen, ''Rapid geometry interrogation for a uniform volume element based Monte Carlo particle transport simulation,'' MS thesis, Montana State University, 1998.
[54] J. S. Hendricks and J. D. Court, ''MCNP4B verification and validation,'' LA-13181, Los Alamos National Laboratory, Los Alamos, 1996.
[55] D. J. Whalen, D. A. Cardon, J. L. Uhle, and J. S. Hendricks, ''MCNP: Neutron benchmark problems,'' LA-12212, Los Alamos National Laboratory, Los Alamos, 1991.
[56] D. J. Whalen, D. E. Hollowell, and J. S. Hendricks, ''MCNP: Photon benchmark problems,'' LA-12196, Los Alamos National Laboratory, Los Alamos, 1991.
[57] K. J. Riley, ''Construction and characterization of a fission converter based epithermal neutron beam for BNCT,'' Ph.D. thesis, Massachusetts Institute of Technology, 2001.
[58] O. K. Harling, K. J. Riley, T. H. Newton, B. A. Wilson, J. A. Bernard, L.-W. Hu, E. J. Fonteneau, P. T. Menadier, S. J. Ali, B. Sutharshan, G. E. Kohse, Y. Ostrovsky, P. H. Stahle, P. J. Binns, and W. S. Kiger III, ''The fission converter based epithermal neutron irradiation facility at the MIT reactor,'' Nucl. Sci. Eng. (in press).
[59] W. A. Rhoades, ''The TORT three-dimensional discrete ordinates neutron/photon transport code,'' ORNL TM-13221, Oak Ridge National Laboratory, June 1996.
[60] See EPAPS Document No. MPHYA6-29-009201 for supporting materials for this article. This document may be retrieved via EPAPS homepage (http://www.aip.org/pubservs/epaps.html) or from ftp.aip.org in the directory/epaps/. See the EPAPS homepage for more information.